# Ru-Ni CATALYST IN THE COMBINED DRY-STEAM REFORMING OF METHANE: THE IMPORTANCE IN THE METAL ORDER ADDITION.

**Andrea Álvarez M, Miguel Ángel Centeno, José Antonio Odriozola.**

*Instituto de Ciencia de Materiales de Sevilla. Centro Mixto Universidad de Sevilla-CSIC. Avenida Americo Vespucio 49. 41092. Sevilla, ESPAÑA*

Abstract

Biogas is one of the main biomass-energy resources. Its use for syngas production with a $H_2/CO$ ratio close to 2 would have huge environmental, social and economic impact in the actual energetic scenario. However, the use of dry reforming, where the two main components are transformed into syngas, does not allow the desired $H_2/CO$ ratio. For this reason, the addition of water is proposed.

The process was performed with two Ru-Ni catalysts where the metal order in the impregnation process was varied.

The catalysts were prepared either by simultaneous or consecutive impregnation of the active phases and its catalytic performance in the combined dry-steam reforming of methane was tested. The catalysts were characterized by FRX, XRD, $S_{BET}$, TPR-$H_2$ and Raman spectroscopy. The existence of a strong Ni-Ru interaction is evidenced by Raman spectroscopy and TPR-$H_2$ in the sample synthesized by the simultaneous impregnation. Concerning the catalytic activity, this sample presents the higher $CH_4$ and $CO_2$ conversion values in the entire composition rate and the lowest amount of carbon deposits after reaction. After pulse, and reactivity tests it was concluded that the higher Ni-Ru interaction displayed by the catalyst synthesized by the simultaneous impregnation, enhances the carbon gasification.

Keywords

Combined steam-dry reforming of methane, syngas, Ru-Ni catalyst.

1. Introduction

The continuous use of fossil fuels as primary energy source has led to numerous social and environmental problems in our planet. Humanity has reached a breaking point where the search of new,

1

renewable and environmental friendly energy suppliers, is an essential task in order to ensure the energetic sustainability of our planet [1, 2].

Although hydrogen as energetic vector is one of the most promising technologies towards a clean and sustainable energetic future [3,4], its infrastructure of production and distribution is not currently available. For this reason, a "bridge" technology, like synthetic fuels produced by Fischer-Tropsch (FT) technology, is a very good option to overcome the actual petroleum scarcity [5].

The first step in the manufacture of synthetic fuels via FT reaction is the production of syngas with a $H_2/CO$ ratio close to 2. This part of the process accounts 60% of the total economic investment, which means, that finding viable, and cheap ways to obtain syngas with a $H_2/CO$ ratio of 2 could increase the profitability of the FT process.

Among the different available methods for syngas production, we can find pyrolysis, partial oxidation, autothermal reforming, dry and steam reforming [6-10]. Nevertheless, besides the chosen method, the selection of the syngas source can determine the viability of the process. The renewable energy sources, such as biomass, are considered highly advantageous regarding the environmental, social and economic legislations.

Biogas, product of the anaerobic digestion of organic matter seems a very good option since its transformation to syngas could give a huge aggregate value to wastes. However in order to use biogas to produce syngas with the desired $H_2/CO$ ratio some issues have to be considered. Dry methane reforming [11-16], where these two mayor greenhouse gases ($CO_2$ around 40% and $CH_4$ around 60%) are transformed, is the perfect reaction to transform biogas into syngas, however, is a very endothermic reaction and requires high operating temperatures (800-1000ºC) to reach high conversions. These very high operating temperatures result in the deactivation by coke deposition mainly due to he deep cracking of methane, which is thermodynamically favored at high temperatures [17]. Furthermore, the syngas produced has always a $H_2/CO$ ratio lower than 1, which makes this process unusable for the production of syngas for the FT process. However, these problems can be solved adding water to feed [18-20] . The carbon formation problem is reduced due to the presence of water and the desirable $H_2/CO$ ratio can be adjusted by optimizing the $CH_4:H_2O:CO_2$ molar ratio. Koo et al. [21, 22] investigated the combination of both reforming processes. They determined that a $H_2/CO$ of 2 could be achieved by a feed ratio of $CH_4:H_2O:CO_2$ of 1:0.8:0.4. Choudhary et al. [23] report the complete conversion of methane towards syngas by the combined dry-steam reforming at 850ºC. Gangadharan et al. [24] evaluated the economic

and environmental impact of the combination of dry and steam reforming. A simulation procedure was carried out using the Aspen Plus® software. Their carbon footprint calculations showed that the combination of both processes implied a less environmental impact. Furthermore, the employment of this combined dry-steam reforming, could be also used to produce syngas from unconventional gas sources (tight gas, shale gas and coalbed methane) that in some cases could reach a $CO_2$ content of about 40% [25-28].

Catalysts used for reforming processes are usually based on Ni. This metal has an excellent activity/price ratio, so high metal loading (~15%) are feasible [18] in order to achieve high catalytic activities. Nevertheless, besides some sintering problems, Ni gets easily deactivated owed to carbon deposits in the surface. In order to avoid this type of deactivation, the modification of the support and the addition of other metals are common strategies to increase the stability of Ni catalysts.

Owing to the fact that the formation of coke in oxide supports is the result of the acid-catalyzed cracking and polymerization reactions between the coke precursors [29], the modifications of the acid-base properties of the support is fundamental. Wang at al. [30] report that the addition of basic elements as Na or Mg reduce the carbon formation in a 13.4%. Horiuchi et al. [31] report that the addition of Na, K, and Mg decreases the carbon formation owed to the lower catalyst capacity to adsorb dissociatively $CH_4$. Penkova et al. [32-34] established an optimum quantity of MgO in 10%, that allowed the modification of the support acidity and improved the Ni dispersion. In regards with the active phase modification, Trimm et al. [35-37] proposed the formation of Ni-M (M= Sn, Ge…) alloys, where the 3d Ni electrons are interacting with the 2p electrons of the other metal, avoiding in this way, the formation of the coke precursor, nickel carbide. Noble metals, like Pt and Ru also improve Ni stability [38-40]. According to the studies for the $CH_4$ dry reforming over Ni-Ru bimetallic catalyst, the strong improvements in the activity and the stability observed on silica supported Ni-Ru catalyst can be attributed to the formation of Ni-Ru bimetallic clusters with surface mainly covered by Ni, leading to an increase in the metallic dispersion of Ni and favoring the formation of more reactive intermediate carbonaceous species [39-41].

Although the support and active phase modification plays an important role in the stability and activity of the final catalyst, the preparation method, precisely, the metal impregnation order, plays an important role in the final catalytic activity. Mukainakano et al. [42-45] reported that the structure of the bimetallic particles can be influenced according to the preparation method.

Thereby, the present research attempts the synthesis of a modified $Ni/Al_2O_3$ catalyst though the modification of the support with MgO and the addition of Ru along with Ni, in order to make it more resistant towards coke deposition. Apart from the study of the influence of metal order addition in the catalytic activity, the addition of different amounts of water to a model biogas with a $CO_2/CH_4$ of 0.4 is performed, in order to find the optimum conditions for the syngas production with a $H_2/CO$ ratio of 2.

2. Experimental

2.1 Catalyst preparation

The support was synthesized by impregnation of $Mg(NO_3)_2 \cdot 6H_2O$ (Aldrich) on γ-Alumina powder (Sasol) in order to obtain a 10 wt % of MgO. This support, named "MAlu" is calcined at 850ºC for 12h.

For the impregnation of the active phases, two routes where chosen. A simultaneous impregnation, where a mixed solution of dissolved $Ni(NO_3)_2 \cdot 6H_2O$ (Aldrich) and $Ru(NO)(NO_3)_3$ (Johnson Matthey) was added to the support MAlu, and a consecutive impregnation, where the support is first impregnated with $Ni(NO_3)_2 \cdot 6H_2O$, dried, calcined at 500ºC for 3h, and afterwards, was impregnated with a solution of $Ru(NO)(NO_3)_3$. Both solids have a final calcination at 500ºC for 3h. In all cases the wt% of Ni is calculated to be 15%, and Ru wt% load is calculated to be 0.5%. The nomenclature of the samples follows the form, X_$a$Ru, where X indicated the impregnation route (S= Simultaneous or C=Consecutive) and "$a$" indicates the Ru wt% load (0.5).

Supported monometallic catalysts were prepared likewise. The sample "Ni/MAlu" refers to the sample impregnated with only 15% Ni into the support MAlu and the sample "0.5Ru/MAlu" refers to the sample with only 0.5%Ru into the support MAlu.

2.2 Catalyst Characterization

The chemical composition of the samples was determined by X-ray fluorescence spectrometry (XRF) in a PANalytical AXIOS PW440 sequential spectrophotometer with a rhodium tube as source of radiation.

The textural properties were studied by $N_2$ adsorption measurements at liquid nitrogen temperature. The experiences were carried out by means of Micromeritics ASAP 2010 equipment. Before analysis, the samples were degassed for 2 h at 250 ºC in vacuum.

4

X-ray diffraction (XRD) analysis was performed on an X'Pert Pro PANalytical Diffractometer. Diffraction patterns were recorded with Cu Kα radiation (40 mA, 45 kV) over a 2θ-range of 10 to 80° and a position-sensitive detector using a step size of 0.05° and a step time of 1s.

The Raman spectra were recorded on a dispersive Horiba Jobin Yvon LabRam HR800 microscope with a 20 mW He-Ne green laser (532.1 nm) without filter and with a 600 g mm$^{-1}$ grating. The microscope used a 50x objective with a confocal pinhole of 1000 μm.

$H_2$-TPRs were carried out in a Micromeritics AutoChem II 2920 equipment with a TCD detector. The analyses were performed on 200 mg of fresh catalyst under 50 ml/min of a 10% $H_2$/Ar mixture. The temperature was increased from room temperature to 850°C at rate of 10 °C/min and left at 850ºC for 3 hours.

TPO post reaction experiments were carried out on 15 mg of spent catalysts using 100 mL min$^{-1}$ of 5% $O_2$ diluted in He. The temperature was increased at 10 °C min$^{-1}$ from room temperature to 900°C. The gas composition at the outlet was analyzed by mass spectroscopy in a PFEIFFER mass spectrum Vacuum Prisma Plus controlled by the Quadera® program. The $m/z$ = 12, 16, 18, 28, 32, 44 and 22 signals were registered.

2.3 Catalytic activity measurement

2.3.1 Combined dry-steam reforming of methane.

The reaction was performed in a computerized commercial Microactivity Reference catalytic reactor (PID Eng&Tech), employing a Hastelloy C-276 tubular reactor (Autoclave Engineers) with 9 mm internal diameter. At the reactor outlet a gas–liquid separator was fitted allowing the analysis of gas and liquid phase products. To avoid flow misdistribution profiles within the reactor, the catalyst powders (100≤φ≤200 μm) were diluted with the same amount of crushed quartz sieved to the same particle size range.

A biogas model stream with a $CO_2$/$CH_4$ ratio of 0.4 was used in order to perform the catalytic test. Variable amounts of water were added to the system in order to achieve the desired $H_2$/CO ratio of 2. The molar ratios where changed as shown in Table 1. Flows where set in order to achieve a space velocity of WHSV=120.000 mL/g.h.

Table 1. Molar $CH_4:H_2O:CO_2$ ratio of the reaction conditions.

| Molar ratio $CH_4:H_2O:CO_2$ | 1: 0.14 : 0.4 | 1: 0.21 : 0.4 | 1: 0.36 : 0.4 | 1: 0.56 : 0.4 |
|---|---|---|---|---|
| Water % | 9 | 13 | 20 | 28 |

Gas products were analyzed on line using a MicroGC (Varian 4900) equipped with Porapak Q and MS-5A columns. Prior to reaction, the catalyst was reduced at 850ºC in 100 mL/min $H_2$ (50%, v/v in inert) for 3 h. The $CH_4$ and $CO_2$ conversion was calculated according to Eq. (1) and (2) respectively where $CH_{4\ in}/CO_{2\ in}$ is the concentration in the inlet and $CH_{4\ out}/CO_{2\ out}$ is the one at the outlet.

$$CH_4\ conversion(\%) = \frac{CH_{4\ in} - CH_{4\ out}}{CH_{4\ in}} \times 100 \quad (1)$$

$$CO_2\ conversion(\%) = \frac{CO_{2\ in} - CO_{2\ out}}{CO_{2\ in}} \times 100 \quad (2)$$

The stability of the samples was tested during 96h varying the amount of water from 20% to 13% then 28% and finally 9%. Each reaction was carried for 24h after which the solid was purged during 30min with $N_2$, and continued the reaction with the water amount changed.


2.3.2 CO pulses and $CH_4$-$CO_2$ alternate pulses.

CO and $CH_4$-$CO_2$ pulses were carried out in a PID Eng&Tech equipment. A conventional U quartz reactor was used with approximately 50mg of sample. The gas composition at the outlet was analyzed by mass spectroscopy in a PFEIFFER mass spectrum Vacuum Prisma Plus controlled by the Quadera® program. The sample is first reduced with 50 ml/min of a 10% $H_2$/Ar mixture. The temperature was increased from room temperature to 850°C at a rate of 10 °C/min and left at 850ºC for 3 hours. Then, an Ar stream cleaned the sample while decreasing the temperature to 750ºC (reaction temperature). After cleaning during 30 minutes, 10 equivalent CO pulses of 1mL where added, after which the sample is again cleaned during 1h with a stream of 50 ml/min of Ar. After this second cleaning, 10 alternate pulses of $CH_4$-$CO_2$ where applied.


2.3.3 Catalytic activity in water gas shift (WGS) reaction at high temperature.

The study of the high-temperature WGS reaction was carried out at 750ºC and atmospheric pressure in a stainless steel fixed bed reactor at 15400 mL/g.h. Prior to reaction the sample was reduced under 100ml/min of a 50% $H_2$-$N_2$ flow at 850ºC for 3h. Four $H_2O$/CO ratios were tested, maintaining always the

6

amount of water and varying the amount of CO. Products and reactants were analyzed by on-line URAS 2G CO, $CO_2$ gas analyzer (ABB A02020). The CO conversion was calculated according to Eq. (3) where $CO_{in}$ is the concentration in the inlet and CO out is the one at the outlet.

$$CO\ conversion(\%) = \frac{CO_{in} - CO_{out}}{CO_{in}} \times 100 \quad (3)$$

## 3. Results and Discussion

### 3.1 Chemical composition and textural properties

Table 2 presents the chemical compositions of the sample and their textural properties. The XRF results show a quiet similar incorporation of the metals in both methods, achieving the desired values of metal phase. The Mg/Al ratio did not change after the impregnation, which implies that the support wasn't modified in the metal impregnation process. A value of Mg/Al=0.12 was maintained, which correspond to a 9.6% of MgO in all the samples. $N_2$ adsorption and desorption isotherms (not shown) are type IV, which are typical for mesoporous solids. Their hysteresis loops are H1 type, which indicates a cylindrical-interconnected type of pores [46, 47]. The addition of Ni and Ru barely changes the textural properties of the modified alumina used as support.

Table 2. Chemical compositions and textural properties

| Sample | Weight % | | Mg/Al | $S_{BET}$ $(m^2/g)$ | Pore volume $(cm^3/g)$ |
|--------|----------|------|-------|------|------|
|        | %Ni | %Ru | | | |
| MAlu | - | - | 0.12 | 123 | 0.37 |
| Ni/MAlu | 17.2 | - | 0.12 | 110 | 0.32 |
| 0.5Ru/MAlu | - | 0.41 | 0.12 | 118 | 0.35 |
| S_0.5Ru | 15.2 | 0.40 | 0.12 | 106 | 0.31 |
| C_0.5Ru | 16.7 | 0.45 | 0.12 | 108 | 0.32 |

### 3.2 X-ray diffraction

Figure 1 shows the diffraction patterns of the different samples. Figure 1_A correspond to the calcined samples. Since before the reaction a reductive treatment is performed in the samples, the reduced samples are also studied. Figure 1_B correspond to the samples after the activation treatment. The support MAlu presents the typical diffraction lines corresponding to the Mg-Al spinel ($MgAl_2O_4$) at 31.2, 45.8, 59.3 and 66.2 °2θ (JCPDS 00-050-0741). There are no peaks corresponding to MgO, which implies the total insertion of Mg into the $Al_2O_3$ lattice forming the $MgAl_2O_4$ spinel.
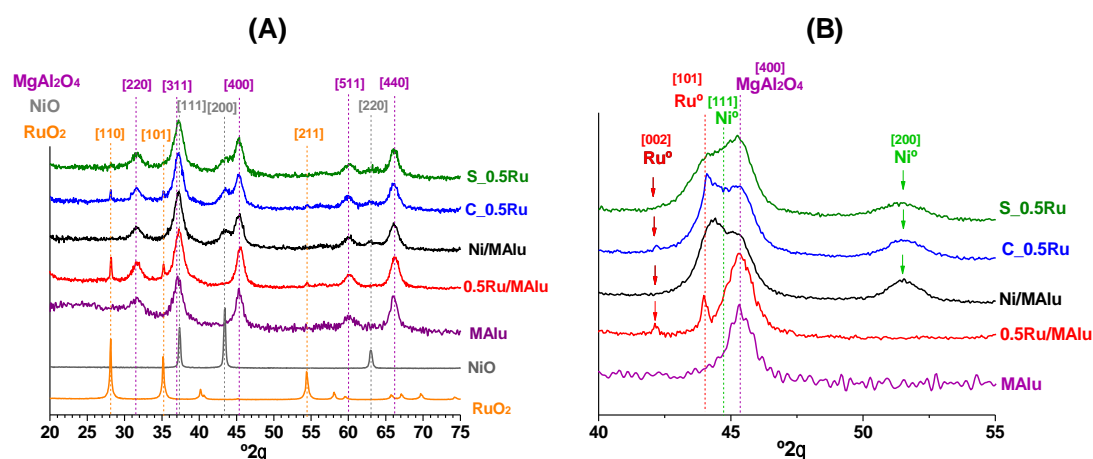
7

Figure 1. Diffraction patterns. (A) Calcined samples (B) Reduced samples.

Although all the XRD patterns are dominated by the support peaks, in the calcined samples (Figure 1_A) Ni is detected as NiO (JCPDS 00-047-1049) and Ru as $RuO_2$ (JCPDS 01-070-2662). All crystallite sizes corresponding to NiO and $RuO_2$ are calculated with Scherrer equation and posted in Table 3. NiO crystallite size is around 6 nm and $RuO_2$ one is around 36 nm except in the sample S_0.5Ru where no presence of $RuO_2$ was found. This could be owed to a better dispersion of $RuO_2$, to the formation of a mixed-oxide Ni-Ru, or even to a possible inclusion of $Ru^{+4}$ in the support lattice.

On the other hand, reduced samples (Figure 1_B) show the peaks of the corresponding metal phases $Ni^0$ (JCPDS 00-004-0850) and $Ru^0$ (JCPDS 00-006-0663). Crystallite size is around 6 nm for Ni and 20 nm for Ru according to Scherrer equation. As observed in the calcined samples, no evidence of any ruthenium species was found in the S_0.5Ru sample, implying a better dispersion of $Ru^0$ or a possible Ni-Ru solid solution. According to the phase diagram of the Ni-Ru system [48], the solid solution, where $Ni^0$ is enriched with $Ru^0$ is possible at the used reduction temperature (850ºC). Nevertheless, Shiraga et al., and Rynkowski et al. [49, 50] reported a clear shift towards lower angles in the Niº peaks which implied the insertion of $Ru^0$ in the $Ni^0$ lattice, however, in the present samples, no shift was observed.

Table 3. Crystallite size, reducibility and dispersion data of the samples.

| Sample | Calcined samples | | Reduced samples | | Reducibility |
|---|---|---|---|---|---|
| | NiO (nm) | $RuO_2$ (nm) | Niº(nm) | Ruº(nm) | % |
| Ni/MAlu | 6.0 | - | 6.0 | - | 74 |
| 0.5Ru/MAlu | - | 35 | - | 25 | 82 |
| C_0.5Ru | 6.3 | 38 | 6.0 | 20 | 79 |
| S_0.5Ru | 5.3 | * | 5.0 | * | 83 |

*= Not observed

3.3 Raman spectroscopy

Raman spectra of the synthesized solids are represented in Figure 2. For clarity, reference solids (RuO$_2$ and NiO) are also included. The support MAlu shows a Raman spectrum where three bands can be noticed at 310, 410 and 720 cm$^{-1}$. As evidenced by XRD the support MAlu is formed by the spinel MgAl$_2$O$_4$. This type of structure has a spatial group Fd3m, which includes 5 active Raman modes [51, 52] (A$_{1g}$ + Eg + 3T$_{2g}$). O'Horo et al. [51] assign the E$_g$ mode to the band towards 410 cm$^{-1}$, the A$_{1g}$ mode to a band located towards 772 cm$^{-1}$ and the 3T$_{2g}$ modes are reported to be found at 311, 492, and 671 cm$^{-1}$. In the current case, the first T$_{2g}$ mode, and the E$_g$ mode are clearly observed, nevertheless, the last wide band towards 720 cm$^{-1}$ could represent the overlapping of the A$_{1g}$ and T$_{2g}$ mode. In regards with the reference samples, the NiO Raman spectra shows a wide band towards 500 cm$^{-1}$ that could be assigned to the two overlapping bands (360 and 527 cm$^{-1}$) that are attributed to first order transverse optical (TO) and longitudinal (LO) phonon modes [53-55] of NiO. The Ni/MAlu sample shows the same spectra profile as NiO but shifted towards higher values. This shift could be attributed to the difference in crystallite size as detected by XRD (Figure 1_A).
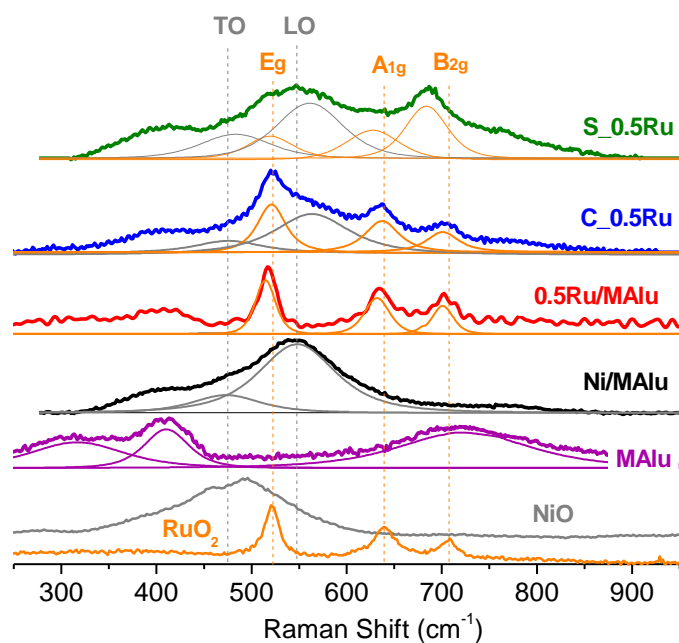


Figure 2. Raman spectra of the samples.

Pure RuO$_2$ has three active Raman modes, corresponding to E$_g$, A$_{1g}$, and B$_{1g}$ at 510, 625 and 700 cm$^{-1}$ as reported in literature [56-59]. The same bands and relative intensities are found in the sample

9

0.5Ru/MAlu and can be distinguished in the C_0.5Ru sample. Nevertheless, the sample S_0.5Ru has a different band distribution; the $B_{2g}$ mode is blue shifted and the intensity ratio of the bands is changed. Although the difference could be attributed to the different crystallite size, this different band distribution could also be attributed to a possible interaction between $Ni^{+2}$ and the $RuO_2$, which disrupts the $RuO_2$ lattice.

 3.4 TPR-$H_2$.

 Figure 3 shows the TPR-$H_2$ of the synthesized samples.  A first reduction peak around 168ºC is observed on the Ru containing ones. This $H_2$ consumption can be ascribed to the reduction of $Ru^{4+}$ to $Ru^0$. Koopman et al. [60] describe the reduction of Ru over $SiO_2$ and report a total reduction of Ru around 275ºC. Nevertheless, they report an hydrogen consumption around 177ºC that they attributed to finely dispersed $RuO_2$. Balin et al. [61] describe the reduction of $RuO_2$ over alumina and reported two reduction peaks. The first one, at 184ºC, was attributed to the reduction of small $RuO_2$ particles while the second one, at 253ºC was ascribed to $RuO_2$ agglomerates.
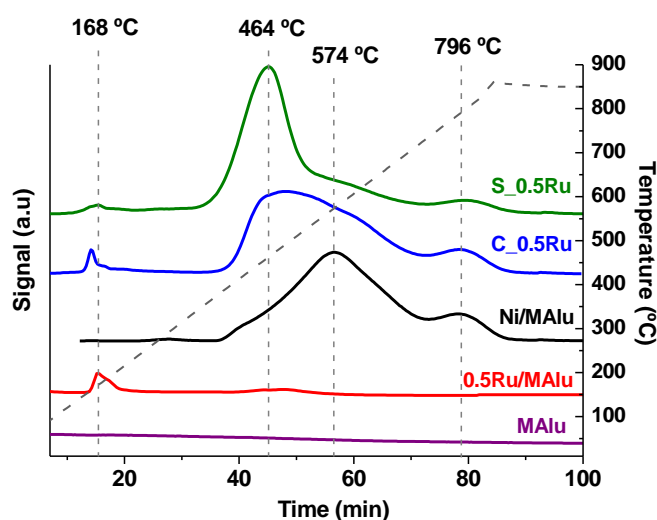


Figure 3. TPR-$H_2$ of the synthesized samples.

 The solids containing Ni present the peak of maximum reduction around 574ºC that correspond to the reduction of NiO [62]. Nevertheless, a shoulder around 796ºC is observed. This $H_2$ consumption can be attributed to the reduction of Ni in strong interaction with the support. Considering that the amount of MgO added to the initial $\gamma$-$Al_2O_3$ support was of 10% and that the total available tetrahedral sites available in the $\gamma$-$Al_2O_3$ accounts for 28%, there are still tetrahedral sites available for Ni where it can interact and form the Ni-Al spinel ($NiAl_2O_4$). The Ni reduction in the $NiAl_2O_4$ spinel has been widely

10

studied [63-65] and has been reported to present Ni reduction peaks around 800ºC. On the other hand, is worth to notice the difference in profile shape between 400-600ºC. The sample S_0.5Ru has higher reduction around lower temperatures (464ºC) than the sample C_0.5Ru. This profile difference stand for the stronger Ni-Ru interaction stated before in the Raman and XRD analysis.

The reducibility values calculated for all the samples are shown in Table 3. As shown, the addition of Ru increased the reducibility of the samples. Enger et al. [66] describe that noble metals are able to promote the reduction of Ni owed to the electronics effects and spillover phenomenon. Enger indicates that an intimate contact between the metals should exist in order to observe this phenomenon.

4. Catalytic activity

4.1 Combined dry-steam reforming of methane.

The $CH_4$ and $CO_2$ conversions are shown in Figure 4. As seen en Figure 4_A, at low water values, $CH_4$ conversion does not exceed the 25%, owed mainly to the low $CH_4/CO_2+H_2O$ ratio (Table 1), which implies that $CO_2$ and $H_2O$ act as limiting reagents. The $CH_4$ conversion increases with the amount of water in the feed, owed mainly to the increasing participation of the steam reforming reaction.

However, the increase of water towards 13% raised the $CO_2$ conversion in the S_0.5Ru sample, although for the other two samples no great difference was found. Further water addition decrease the $CO_2$ conversion owed mainly to the participation of the RWGS reaction. As expected, the addition of water to the $CO_2$-$CH_4$ mixture, increased the $H_2/CO$ ratio owed mainly to higher amount of $H_2$ produced by the RWGS reaction, achieving the desired value of $H_2/CO=2$ when adding a 28% of water in the model biogas stream.
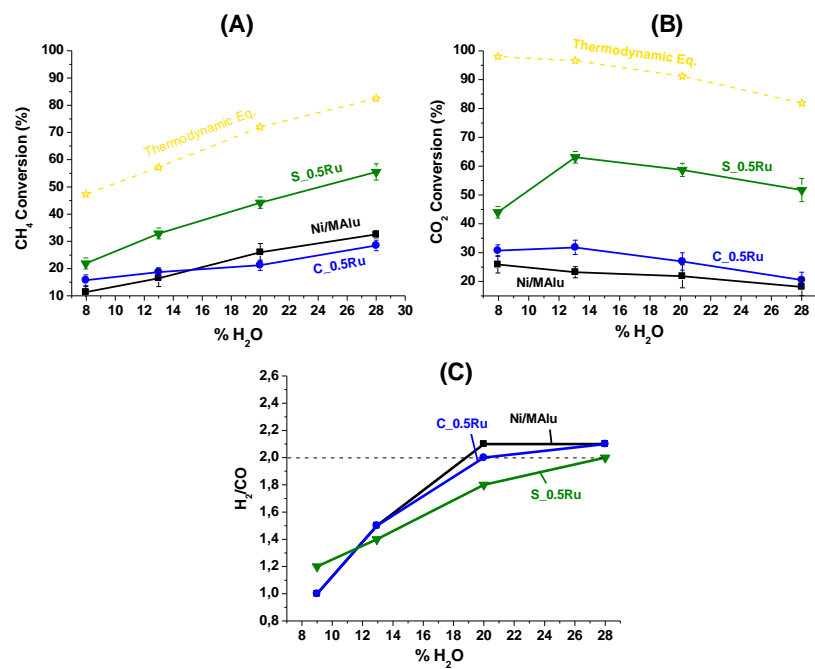
11

Figure 4. (A) $CH_4$ conversion. (B) $CO_2$ conversion. (C) $H_2/CO$ in the dry-steam reforming of methane changing the water % in the feed at 750ºC.

The $CH_4$ and $CO_2$ conversions and $H_2/CO$ ratio obtained from the stability test are shown in Figure 5. The results of activity each 24h are maintained and match the ones obtained previously (Figure 4), indicating the reproducibility of the reaction.
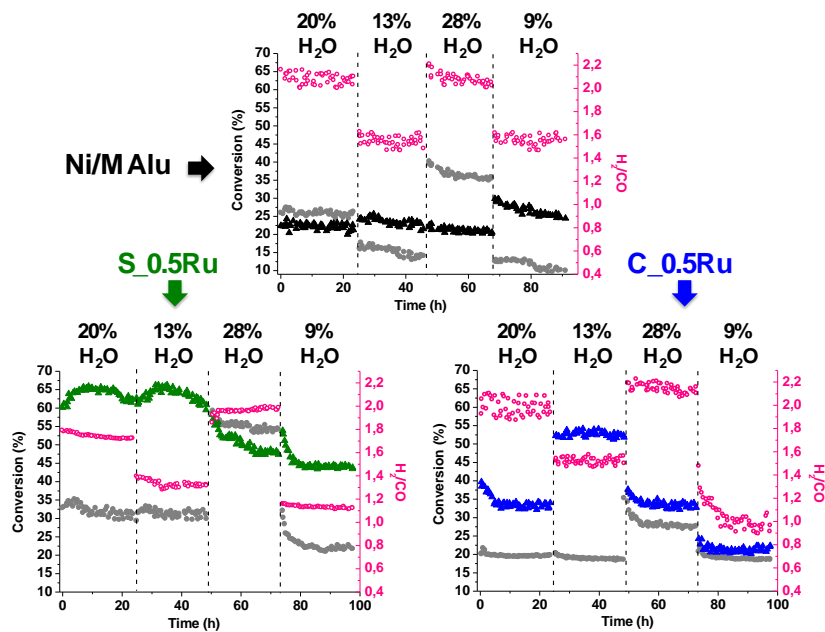


Figure 5. (●) $CH_4$ conversion. (Δ Δ Δ) $CO_2$ conversion. (O) $H_2/CO$ in the dry-steam of methane during 96h at 750ºC.

12

As seen in Figure 5, there is no evidence of a clear deactivation process. However, the analysis of the post-reacted samples by TPO (Figure 6) showed clear differences. All samples show an increase in the $CO_2$ signal (Figure 6_A) towards 604ºC which can be attributed to the presence of amorphous carbon in the sample [67] although the sample Ni/MAlu showed a signal towards higher temperature, which can be owed to the presence of more structured carbon. Nevertheless, is worth to mention, that the sample S_0.5Ru showed the lowest amount of $CO_2$, which can be related to the lowest amount of carbon deposits in the sample.
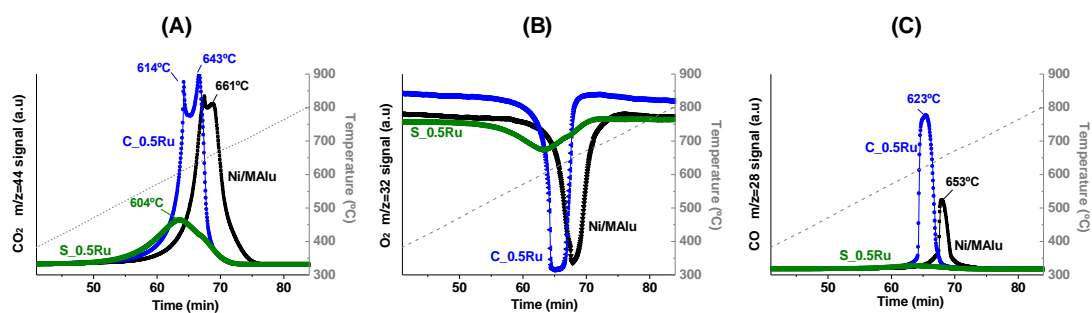


Figure 6. TPO analysis of the post-reacted samples. (A) $CO_2$ signal. (B) $O_2$ signal and (C) CO signal.

On the other hand, an interesting fact occurred to the samples C_0.5Ru and Ni/MAlu. Around 623ºC the $O_2$ is totally consumed by the sample (Figure 6_B) and the carbon present in the sample starts to be gasified by the $CO_2$ by Boudouard reaction, giving the signal of CO represented in Figure 6_C. This behavior can be related to the elevated amount of carbon in the sample, and is worth to mention that the sample C_0.5Ru presents a higher signal of $CO_2$ and a higher production of CO, which can confirm that this sample, even with the Ru presence, has the higher amount of carbon.

4.2 CO pulses and $CH_4$-$CO_2$ alternate pulses.

Two of the main responsible reactions of the coke formation in Ni catalyst are the Boudouard reaction and the $CH_4$ decomposition. Thus, in order to evaluate the difference of the samples in these reactions, some experiment of CO pulses and $CH_4$-$CO_2$ alternate pulses were performed.

Figure 7 shows the $CO_2$ signal after each CO pulse. As seen, all samples present a $CO_2$ signal, which means that all are active in the Boudouard reaction. However, there is a big difference; the samples with 0.5%Ru show almost the same $CO_2$ profile, whereas the Ni/MAlu sample shows lower $CO_2$ signal, implying that, in the tested catalysts, Ru is the main responsible of the CO disproportionation [68-70].
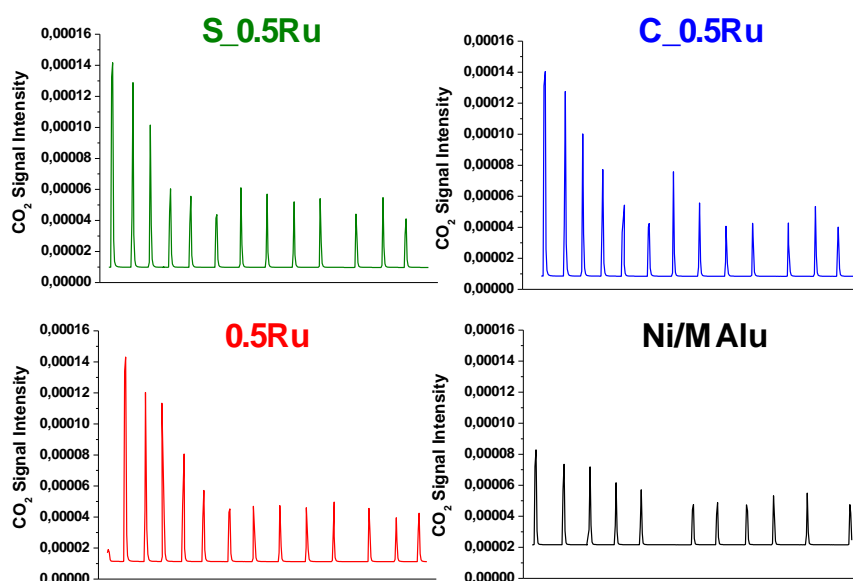
13

Figure 7. $CO_2$ signal after each CO pulse.

Regarding the alternate $CH_4$-$CO_2$ pulses, the $H_2$ and CO signals after each pulse are represented in Figure 8. The increase in the amount of $H_2$ after de first $CH_4$ pulse in the samples containing Ni indicates that this metal is the one responsible of the $CH_4$ decomposition as reported in literature [12, 70]. Although Ru has been also responsible for $CH_4$ cracking [18, 71], there was no evidence of this behavior under these conditions.
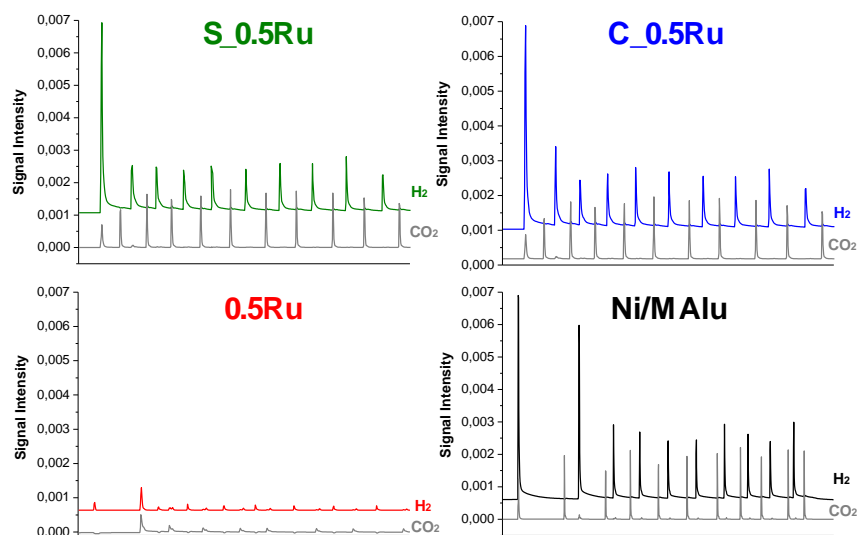


Figure 8. $H_2$ and CO signals after the $CH_4$ and $CO_2$ pulses.

4.3 Catalytic activity in water gas shift (WGS) reaction at high temperature.

Since after the pulse experiments no clear conclusions about the difference of the amount of carbon deposits evidenced in Figure 6 were obtained, a WGS experiment was performed in order to evaluate the activity of the catalyst when reacting CO and $H_2O$. Figure 9 shows the CO conversion at 750°C at different $H_2$/CO ratios. The sample Ni/MAlu presents the lowest activity and remained under the WGS equilibrium curve. However, the sample C_0.5Ru shows higher activity, and overcome the WGS equilibrium curve, which can be explained by the gasification of carbon from the Boudouard reaction when CO gets to the catalyst surface. Nevertheless, the catalyst S_0.5Ru has a conversion higher than 90% when working with lower contents of water, and increase towards complete CO conversion when raising the amount of water. This high capacity of carbon gasification could explain the big difference in the amount of carbon deposits evidenced in Figure 6.
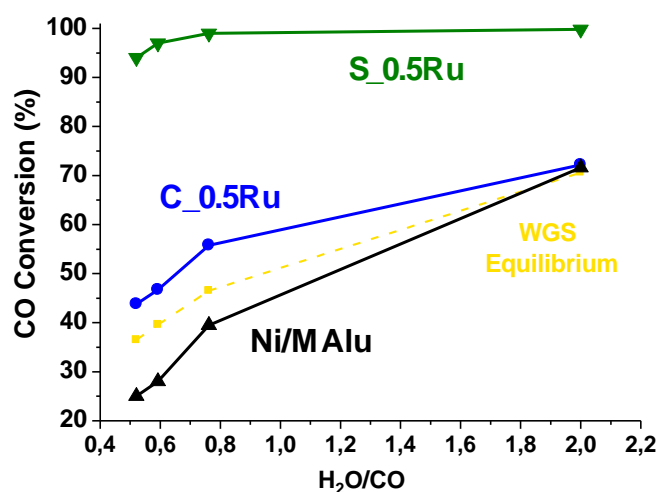


Figure 9. CO conversion at 750°C at different $H_2O$/CO ratios.

As observed in Figure 4, the catalyst S_0.5Ru presents the high catalytic activity in all the water % range and also, is the sample that presents the less amount of carbon deposited in the sample after reaction. The better Ru dispersion which implies a better Ru-Ni interaction, evidenced by Raman and TRP could explain the better catalytic performance of the sample, implying that, in this kind of systems the metal order addition is critical.

5. Conclusions

Two Ru-Ni catalysts where prepared using a modified $Al_2O_3$ as support. For the active phase impregnation, two methods were employed. A simultaneous method were the two metals were impregnated at the same time, and a consecutive method, were the support is first impregnated with Ni, calcined, and then impregnated with Ru.

The physicochemical characterization show that the extent of incorporation of Ni and Ru was similar in both routes and the desired metal values were achieved. There were no significant differences in the textural properties of the support after the metal impregnation. However, XRD, Raman and TPR-$H_2$ analysis showed clear differences in the samples depending on the metal impregnation order. There was no evidence of Ru species in the XRD analysis of the sample S_0.5Ru indicating a higher Ru dispersion. Moreover, Raman and TPR-$H_2$ analysis showed that the Ni-Ru interaction in this sample is bigger than in the C_0.5Ru.

Concerning the catalytic activity, the desired $H_2/CO$ ratio of 2 was achieved thought the addition of water to a model biogas with a $CO_2/CH_4$ ratio of 0.4, using a molar $CH_4:H_2O:CO_2$ ratio of 1:0.56:0.4 and a temperature of 750ºC. The sample S_0.5Ru exhibit the highest catalytic activity and lowest tendency to coke depositions owed to the fact that the good Ru-Ni interaction makes it the most active sample in the gasification of carbon deposits

7. References

1. Boudghene Stambouli A, Traversa E (2002) Fuel cells, an alternative to standard sources of energy. Renewable and Sustainable Energy Reviews 6:295–304.

2. Dry ME (2001). High quality diesel via the Fischer-Tropsch process. Journal of Chemical Technology and Biotechnology 77:43–50.

3. Stambouli AB (2002) Fuel cells: The expectations for an environmental-friendly and sustainable source of energy. Renewable and Sustainable Energy Reviews 15:4507–4520.

4. Stambouli AB, Traversa E (2002) Solid oxide fuel cells (SOFCs): a review of an environmentally clean and efficient source of energy. Renewable and Sustainable Energy Reviews 6:433–455.

5. Sousa-Aguiar EF, Appel LG, Mota C (2005) Natural gas chemical transformations: The path to refining in the future. Catalysis Today 101:3–7.

6. Froment GF (2000) Production of synthesis gas by steam and $CO_2$ reforming of natural gas. Journal of Molecular Catalysis A: Chemical 163:147–156.

7. Angeli SD, Monteleone G, Giaconia A, Lemonidou AA (2014) State-of-the-art catalysts for $CH_4$ steam reforming at low temperature. International Journal of Hydrogen Energy: 39:1979–1997.

8. Xu J, Froment GF (1989) Methane steam reforming, methanation and water-gas shift: I. Intrinsic kinetics. AIChE J 35:88–96.

9. Oliveira ELG, Grande CA, Rodrigues AE (2009) Steam methane reforming in a $Ni/Al_2O_3$ catalyst: Kinetics and diffusional limitations in extrudates. Canadian Journal of Chemical Engineering 87:945–956.

10. Rostrup-Nielsen JR (1994) Catalysis and large-scale conversion of natural gas. Catalysis Today 21:257–267.

11. Guczi L, Erdohelyi A (2012) Catalysis for alternative energy Generation. Springer Ed. 1–543.

12. Bradford MCJ, Vannice MA (1999) Review. $CO_2$ Reforming of $CH_4$. Catalysis Reviews 41:1–42.

13. Bradford MCJ, Vannice MA (1996) Review. Catalytic reforming of $CH_4$ with $CO_2$. II. Reaction Kinetics. Applied Catalysis A: General 142:97–122.

14. Bradford MCJ, Vannice MA (1999) $CO_2$ Reforming of $CH_4$ over supported Ru Catalysts. Journal of Catalysis 183:69–75.

15. Bradford MCJ, Vannice MA (1999) The role of metal-support interactions in $CO_2$ reforming of $CH_4$. Catalysis Today 50:1–10.

16. Wang HY, Ruckenstein E (2000) Carbon dioxide reforming of methane to synthesis gas over supported rhodium catalyst: the effect of support. Applied Catalysis A: General 204:143–152.

17. Ryi S-K, Lee S-W, Park J-W, et al. (2013) Combined steam and $CO_2$ reforming of methane using catalytic nickel membrane for gas to liquid (GTL) process. Catalysis Today 1–8.

18. Rostrup-Nielsen J (1984) Catalytic Steam Reforming. In: Anderson J, Boudart M (eds) Catalysis. Springer Berlin Heidelberg, pp 1–117

19. Rostrup-Nielsen JR (2000) New aspects of syngas production. Catalysis Today 63:159–164.

20. Rostrup-Nielsen JR, Sehested J (2002) Review. Hydrogen and Synthesis Gas by Steam and $CO_2$ reforming. Advanced Synthesis & Catalysis 47:65–139.

21. Koo KY, Roh H-S, Jung UH, et al. (2009) Combined $H_2O$ and $CO_2$ reforming of $CH_4$ over nano-sized $Ni/MgO-Al_2O_3$ catalysts for synthesis gas production for gas to liquid (GTL): Effect of Mg/Al mixed ratio on coke formation. Catalysis Today 146:166–171.

22. Koo KY, Roh H-S, Jung UH, Yoon WL (2012) Combined $H_2O$ and $CO_2$ reforming of $CH_4$ over Ce-promoted $Ni/Al_2O_3$ catalyst for gas to liquid (GTL) process: Enhancement of $Ni–CeO_2$ interaction. Catalysis Today 185:126–130.

23. Choudhary VR, Rajput AM (1996) Simultaneous Carbon Dioxide and Steam Reforming of Methane to Syngas over $NiO−CaO$ Catalyst. Industrial & Engineering Chemistry Research 35:3934–3939.

24. Gangadharan P, Kanchi KC, Lou HH (2012) Evaluation of the economic and environmental impact of combining dry reforming with steam reforming of methane. Chemical Engineering Research and Design 90:1956–1968. 8

25. Islam MR (2015) Chapter 3 - Important Features of Unconventional Gas. In: Islam MR (ed)

Unconventional Gas Reservoirs. Gulf Professional Publishing, Boston, pp 71–127

26. Holditch SA (2013) Unconventional oil and gas resource development – Let's do it right. Journal of Unconventional Oil and Gas Resources 1–2:2–8.

27. Weijermars R, Drijkoningen G, Heimovaara TJ, et al. (2011) Unconventional gas research initiative for clean energy transition in Europe. Journal of Natural Gas Science and Engineering 3:402–412.

28. McGlade C, Speirs J, Sorrell S (2013) Unconventional gas – A review of regional and global resource estimates. Energy 55:571–584.

29. Bartholomew CH (2001) Mechanisms of catalyst deactivation. Applied Catalysis A: General 212:17–60.

30. Wang S, Lu GQM (2000) Effects of promoters on catalytic activity and carbon deposition of Ni/$\gamma$-$Al_2O_3$ catalysts in $CO_2$ reforming of $CH_4$. Journal of Chemical Technology and Biotechnology 75:589–595.

31. Horiuchi T, Sakuma K, Fukui T, et al. (1996) Suppression of carbon deposition in the $CO_2$-reforming of $CH_4$ by adding basic metal oxides to a $Ni/Al_2O_3$ catalyst. Applied Catalysis A: General 144:111–120.

32. Penkova A, Bobadilla L, Ivanova S, et al. (2011) Hydrogen production by methanol steam reforming on NiSn/MgO-$Al_2O_3$ catalysts: The role of MgO addition. Applied Catalysis A: General 392:184–191.

33. Bobadilla LF, Penkova A, Romero-Sarria F, et al. (2014) Influence of the acid-base properties over NiSn/MgO-$Al_2O_3$ catalysts in the hydrogen production from glycerol steam reforming. International Journal of Hydrogen energy:39:5704–5712.

34. Bobadilla LF, Palma S, Ivanova S, et al. (2013) Steam reforming of methanol over supported Ni and Ni–Sn nanoparticles. International Journal of Hydrogen energy:38:6646–6656.

35. Trimm DL (1999) Catalysts for the control of coking during steam reforming. Catalysis Today 49:3–10.

36. Trimm DL (1997) Coke formation and minimisation during steam reforming reactions. Catalysis Today 37:233–238.

37. Rostrup-Nielsen J, Trimm DL (1977) Mechanisms of carbon formation on nickel-containing catalysts. Journal of Catalysis 48:155–165.

38. de Miguel SR, Vilella IMJ, Maina SP, et al. (2012) Influence of Pt addition to Ni catalysts on the catalytic performance for long term dry reforming of methane. Applied Catalysis A: General 435–436:10–18.

39. Jeong JH, Lee JW, Seo DJ, et al. (2006) Ru-doped Ni catalysts effective for the steam reforming of methane without the pre-reduction treatment with $H_2$. Applied Catalysis A: General 302:151–156.

40. Crisafulli C, Scirè S, Minicò S, Solarino L (2002) Ni-Ru bimetallic catalyst for the $CO_2$ reforming of methane. Applied Catalysis A: General 225:1–9.

41. Crisafulli C, Maggiore R, Minicò S, Galvagno S (1999) $CO_2$ reforming of methane over Ni-Ru catalyst and Ni-Pd bimetallic catalyst. Catalysis Letters 59:21–26.

42. Mukainakano Y, Yoshida K, Kado S, et al. (2008) Catalytic performance and characterization of Pt–Ni bimetallic catalysts for oxidative steam reforming of methane. Chemical Engineering Science 63:4891–4901.

43. Mukainakano Y, Yoshida K, Okumura K, et al. (2008) Catalytic performance and QXAFS analysis of Ni catalysts modified with Pd for oxidative steam reforming of methane. Catalysis Today 132:101–108.

44. Mukainakano Y, Li B, Kado S, et al. (2007) Surface modification of Ni catalysts with trace Pd and Rh for oxidative steam reforming of methane. Applied Catalysis A: General 318:252–264.

45. Yoshida K, Okumura K, Miyao T, et al. (2008) Oxidative steam reforming of methane over Ni/α-Al$_2$O$_3$ modified with trace Pd. Applied Catalysis A: General 351:217–225.

46. Leofanti G, Padovan M, Tozzola G, Venturelli B (1998) Surface area and pore texture of catalyst. Catalysis Today 41:1–13.

47. Condon JB (2006) Surface Area and Porosity Determinations by Physisorption. Measurements and Theory. 1–297.

48. Danilenko VM, Velikanova TY, Mazhuga TG, et al. (1999) Thermodynamic simulation of the Ni—Ru binary-system phase diagram. Powder Metallurgy and Metal Ceramics 38:254–260.

49. Shiraga M, Li D, Atake I, et al. (2007) Partial oxidation of propane to synthesis gas over noble metals-promoted Ni/Mg(Al)O catalysts—High activity of Ru–Ni/Mg(Al)O catalyst. Applied Catalysis A: General 318:143–154.

50. Rynkowski JM, Paryjczak T, lenik M (1995) Characterization of Alumina supported Ni Ru Systems. Applied Catalysis A: General 126:257–271.

51. O'Horo MP, Frisillo AL, White WB Lattice vibrations of MgAl$_2$O$_4$ spinel. Journal of Physics and Chemistry of Solids 34:23–28.

52. Minh NV, Yang I-S (2004) A Raman study of cation-disorder transition temperature of natural MgAl2O4 spinel. The 2nd International Conference on Advanced Vibrational Spectroscopy (ICAVS-2) 35:93–96.

53. Yadav SK, Jeevanandam P (2014) Synthesis of NiO–Al$_2$O$_3$ nanocomposites by sol–gel process and their use as catalyst for the oxidation of styrene. Journal of Alloys and Compounds 610:567–574.

54. Wang W, Liu Y, Xu C, et al. (2002) Synthesis of NiO nanorods by a novel simple precursor thermal decomposition approach. Chemical Physics Letters 362:119–122.

55. Zhu G, Xi C, Xu H, et al. (2012) Hierarchical NiO hollow microspheres assembled from nanosheet-stacked nanoparticles and their application in a gas sensor. RSC Advances 2:4236–4241.

56. Kim MH, Baik JM, Lee SJ, et al. (2010) Growth direction determination of a single RuO$_2$ nanowire by polarized Raman spectroscopy. Applied Physical Letters 96:213108.

57. Meng L, Teixeira V, Santos dos MP (2003) Raman spectroscopy analysis of magnetron sputtered RuO$_2$ thin films. Thin Solid Films 442:93–97.

58. Korotcov A, Hsu HP, Huang YS, et al. (2007) Deposition and characterization of 1D RuO2 nanocrystals by reactive sputtering. Journal of Alloys and Compounds 442:310–312.

59. Huang YS, Pollak FH (1982) Raman Spectroscopy of RuO$_2$. Solid State Communications 43:921–924.

60. Koopman PGJ, Kieboom APG, van Bekkum H (1981) Characterization of Ruthenium Catalyst as Studied by Temperature Programmed Reduction. Journal of Catalysis 69:172–179.

61. Balint I, Miyazaki A, Aika K-I (2003) Chemical and morphological evolution of supported Ru nanoparticles during oxidative conversion of methane. Reaction Kinetics and Catalysis Letters

80:81–87.

62. Qiu Y, Chen J, Zhang J (2007) Effects of MgO promoter on properties of Ni/Al$_2$O$_3$ catalysts for partial oxidation of methane to syngas. Frontiers of Chemical Science and Engineering 1:167–171.

63. Dieuzeide ML, Iannibelli V, Jobbagy M, Amadeo N (2012) Steam reforming of glycerol over Ni/Mg/γ-Al2O3 catalysts. Effect of calcination temperatures. International Journal of Hydrogen energy:37:14926–14930.

64. Salehi E, Azad FS, Harding T, Abedi J (2010) Production of hydrogen by steam reforming of bio-oil over Ni/Al$_2$O$_3$ catalysts: Effect of addition of promoter and preparation procedure. Fuel Processing Technology 92:2203–2210.

65. de Sousa FF, de Sousa HSA, Oliveira AC, et al. (2011) Nanostructured Ni-containing spinel oxides for the dry reforming of methane: Effect of the presence of cobalt and nickel on the deactivation behaviour of catalysts. International Journal of Hydrogen energy: 1–12.

66. Enger B, Lødeng R, Holmen A (2010) Effects of Noble Metal Promoters on In Situ Reduced Low Loading Ni Catalysts for Methane Activation. Catalysis Letters 134:13–23.

67. Li C, Brown TC (2001) Carbon Oxidation Kinetics from evolved carbon oxide analysis during temperature programmed oxidation. Carbon 39:725–732.

68. Shincho E, Egawa C, Naito S, Tamaru K (1985) The behaviour of carbon species produced by CO disproportionation on Ru(1, 1, 10) and Ru(001) surfaces. Surface Science 155:153–164.

69. Shincho E, Egawa C, Naito S, Tamaru K (1985) The behaviour of CO adsorbed on Ru(1,1,10) and Ru(001); the dissociation of CO at the step sites of the Ru(1,1,10) surface. Surface Science 149:1–16.

70. Freund HJ, Messmer RP (1986) On the bonding and reactivity of CO$_2$ on metal surfaces. Surface Science 172:1–30.

71. Wei J, Iglesia E (2004) Isotopic and kinetic assessment of the mechanism of reactions of CH$_4$ with CO$_2$ or H$_2$O to form synthesis gas and carbon on nickel catalysts. Journal of Catalysis 224:370–383.